ORIGINAL PAPER

CH$_4$ and CH$_2$O Oxidation in Lean Gas Engine Exhaust Using Fe$_2$O$_3$ Catalysts
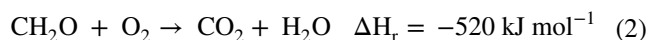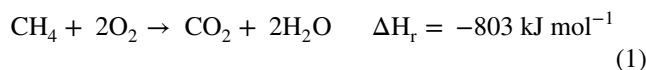
M. Mehne[1] · S. Kureti[1]

Abstract

A systematic series of commercial α-Fe$_2$O$_3$ catalysts was investigated with respect to the after-treatment of the lean exhaust emissions of gas engines. The samples were physico-chemically characterized by X-ray diffraction, Laser Raman spectroscopy, N$_2$ physisorption, temperature-programmed reduction with CO and the temperature-programmed desorption of CO$_2$, whereas the catalytic efficiency was evaluated using a model exhaust gas. Structure–activity correlations showed that for the oxidation of CH$_4$ the number of active Fe sites and the availability of surface and subsurface oxygen are crucial properties of the catalysts. By contrast, the conversion of CH$_2$O is driven by the CO$_2$ adsorption capacity and the amount of OH surface species, in line with the mechanistic understanding gained by step function experiments and diffuse reflectance infrared Fourier-transform spectroscopy (DRIFTS). The in-situ DRIFTS studies suggested that the CH$_2$O oxidation follows a Cannizzaro-type mechanism including the reaction of two CH$_2$O molecules with a surface OH site to form CH$_3$OH and formate species. The subsequent conversion of the formate moieties with H$_2$O results in the reconstruction of the OH groups and the release of formic acid. The latter is assumed to decompose into CO$_2$ and H$_2$ which finally oxidizes to H$_2$O. The best iron oxide catalyst was upscaled to the level of a real catalytic converter, which was tested in the lean exhaust gas of a 600 kW biomethane engine. As a result, the catalyst demonstrated high activity with regard to CH$_2$O and CO removal above 300 and 500 °C, respectively, while only negligible conversion of CH$_4$ occurred.

Keywords Gas engine exhaust · CH$_4$ and CH$_2$O oxidation · Iron oxide · Catalyst · Cannizzaro mechanism

1 Introduction

The emission of greenhouse gases (GHGs) is considered with great concern around the world, and accordingly a multitude of strategies are currently being developed to contain global climate change. Lean-burn gas engines can provide a relevant contribution to the sustainable supply of energy and transportation due to their high efficiency and GHG neutrality, particularly when biomethane is used as a fuel. However, one issue affecting lean gas engines is the emission of methane (CH$_4$) and formaldehyde (CH$_2$O) resulting from the incomplete combustion of the fuel [1–3]. The environmental relevance of these pollutants is associated with the strong GHG impact of CH$_4$ (CO$_2$ factor 25) and the toxicity and carcinogenicity of CH$_2$O [4]. Therefore, emission limits have been introduced in the European Union requiring the after-treatment of gas engine exhaust emissions. For this purpose, catalysts based on platinum (Pt) and palladium (Pd) are considered due to their high oxidation efficiency (Eq. 1 and 2) [5, 6].

$$CH_4 + 2O_2 \rightarrow CO_2 + 2H_2O \qquad \Delta H_r = -803 \text{ kJ mol}^{-1} \tag{1}$$

$$CH_2O + O_2 \rightarrow CO_2 + H_2O \quad \Delta H_r = -520 \text{ kJ mol}^{-1} \tag{2}$$

However, precious metal catalysts only exhibit limited long-term stability for CH$_4$ oxidation [7]. Hence, alternative catalytic materials have been investigated such as Co [8–10], Cu [11, 12] and Mn [8, 10]. By contrast, only little is known about the CH$_4$ oxidation activity of Fe-based catalysts, although iron is characterized by high availability, a low price and toxicological harmlessness. Recently, it was demonstrated that iron catalysts are basically capable

✉ S. Kureti
   kureti@iec.tu-freiberg.de

[1] Institute of Energy Process Engineering and Chemical Engineering, Chair of Reaction Engineering, Technical University of Freiberg, Fuchsmuehlenweg 9, 09599 Freiberg, Germany

of oxidizing CH_4 with a conversion rate of 50% at 500 °C (4000 ppm CH_4, 10 vol% O_2, N_2 balance; 50,000 h^{-1}) [8]. Additionally, iron oxides have been reported as effective catalysts for the oxidation of CO, hydrocarbons and soot under O_2-rich conditions [13–16].

The objective of the present study is the knowledge-based development of advanced iron oxide catalysts for the oxidation of CH_4 and CH_2O in lean gas engine exhaust. For this purpose, a systematic series of commercial iron oxide powder samples was characterized physico-chemically and tested in a model exhaust gas to evaluate structure–activity correlations. The most effective sample was transferred to the honeycomb level for practical laboratory tests followed by up-scaling to a real catalytic converter for tests on a stationary gas engine. Finally, mechanistic studies on CH_2O oxidation were performed with the best catalyst using in-situ diffuse reflectance infrared Fourier transform spectroscopy (DRIFTS) and step-function experiments.

2 Experimental

2.1 Physico-Chemical Characterization of the Samples

In this study, five commercial iron oxide powder samples (Lanxess) with different physico-chemical properties were used. The samples were present in the form of a α-Fe_2O_3 modification, which is thermodynamically stable under the lean exhaust conditions of stationary gas engines, primarily involving temperatures above 450 °C [17]. Before physico-chemical characterization and catalytic testing, each material was pre-treated in air at 600 °C for 3 h (raising the heating at a rate of 4.5 K min^{-1}). The samples were characterized by N_2 physisorption, X-ray diffraction (XRD), Laser Raman spectroscopy, energy dispersive X-ray spectroscopy (EDX), the temperature-programmed reduction of CO (CO-TPR) and the temperature-programmed desorption of CO_2 (CO_2-TPD).

N_2 physisorption was performed on a TriStar II (Micromeritics) at -196 °C. The samples were pretreated at 350 °C for 16 h in a vacuum (10^{-4} bar). The BET surface area (S_{BET}) was calculated from the adsorption data recorded at p/p_0 ratios between 0.06 and 0.20.

XRD was carried out on a D8 Discover (Bruker) at room temperature. The diffractometer was equipped with a Bragg–Brentano configuration, an Fe-filtered Co-Kα radiation source (35 kV/45 mA) and a VANTED-1 detector. Each diffractogram was recorded from 20° to 80° (2Θ) with a step width of 0.01° and dwell time of 0.05 s $step^{-1}$. TOPAS software (Bruker) was used to estimate the crystallite size (d_{cryst}) according to the Scherrer equation.

Laser Raman spectra (LRS) were recorded with an inVia (Renishaw). The spectrometer was equipped with a Nd:YAG laser (532 nm, 127 kW m^{-2}), grating with 1800 lines per mm and a CCD array detector. Spectra were taken between 56 and 1600 cm^{-1} with a resolution of 1.6 cm^{-1}, an exposure time of 60 s and a laser power of 0.5%. Spectral data were processed using WIRE 4.2 software.

EDX was conducted on a Quanta 250 FEG from FEI equipped with an energy dispersive X-ray spectrometer (EDAX AMETEK—Octane Plus) providing a local resolution of about 1.7 nm (dwell time 200 μs). A tungsten incandescent cathode was taken as an electron source with an acceleration voltage of 20 kV. For analysis, the samples were prepared on standard carbon adhesive tabs. EDX measurements were evaluated with the EDAX TEAM software.

CO-TPR and CO_2-TPD were made on a home-made laboratory test bench requiring a quartz glass tube reactor (i.d.: 8 mm). The gases (Air Liquide) were fed by independent mass flow controllers (Bronkhorst), whereas the total flow was always kept at 150 ml min^{-1} (STP). Online gas-phase analysis was performed by a hot measuring FTIR spectrometer (Multi-Gas 2030, MKS instruments). For CO-TPR, a sample mass of 100 mg (powder) was introduced into the reactor as a fixed bed, pre-treated for 15 min at 550 °C in synthetic air flow and then cooled to 50 °C. Subsequently, the TPR was started by continuously dosing a mixture of 3000 ppm CO and N_2 (balance) and raising the temperature to 850 °C at 10 K min^{-1}. Temperatures were controlled by using K-type thermocouples in front of and behind the packed bed ($\Delta T < 5$ K). For CO_2-TPD, the sample used was in the form of granules (500 mg, 125–250 μm). After the same pre-treatment as for CO-TPR, the sample was saturated with CO_2 at 50 °C using a mixture of 3000 ppm CO_2 and N_2 (balance). After this, it was flushed with N_2 until the proportion of CO_2 was below 5 ppm, then TPD was started by heating to 850 °C at the rate of 20 K min^{-1}.

2.2 Catalytic Studies

Catalytic investigations of powders and honeycombs were performed on a laboratory test bench. The powder catalysts (300 mg, particle size < 250 μm) were fixed in the tubular quartz glass reactor (i.d.: 10 mm) with quartz wool, while temperature was monitored by K-type thermocouples located directly in front of and behind the catalyst. Gases were dosed using independent mass flow controllers (Bronkhorst). Gas-phase analysis was carried out as for TPD and TPR, whereas O_2 was measured by a lambda probe (LSU 4.9, Bosch). Reactor inlet concentrations were adjusted by bypassing the reactor. Before the tests, each sample was heated for 15 min at 550 °C in a flowing mixture of 20 vol% O_2 and 80 vol% N_2. Subsequently, the model exhaust gas, composed of 1000 ppm CH_4, 100 ppm CH_2O, 5 vol% O_2, 10 vol%

H$_2$O and N$_2$ (balance), was dosed with a total flow rate of 1000 ml min^{-1} (STP), corresponding to a space velocity (S.V.) of 150,000 h^{-1}. Catalytic data were recorded under stationary conditions, while the temperature was decreased from 550 °C to 200 °C in steps of 50 K.

The best catalyst was coated on a cylindrical cordierite honeycomb (D: 25 mm, L: 40 mm, 400 cpsi) resulting in a load of 100 g l^{-1}. For this purpose, the powder catalyst was dispersed in H$_2$O using hydroxyethylcellulose (Sigma-Aldrich) as detergent (2 g l^{-1}). Subsequently, the honeycomb was dipped into the dispersion and was then dried at 100 °C. This procedure was repeated several times. The honeycomb was finally annealed at 400 °C in air to remove the detergent. The catalytic test procedure was very similar to that for powders, whereas the quartz glass reactor had an i.d. of 26 mm and the total flow was 22.5 l min^{-1} (STP) corresponding to a S.V. of 65,000 h^{-1}. The model exhaust gas consisted of 1500 ppm CH$_4$, 100 ppm CH$_2$O, 600 ppm CO, 250 ppm NO, 5 vol% O$_2$, 12 vol% H$_2$O, 12 vol% CO$_2$ and N$_2$ (balance).

The best catalyst was transferred to a real-size honeycomb (D: 390 mm, L: 450 mm, 200 cpsi) producing a loading of 85 g l^{-1}. The coating was done as described in previous paragraph. The tests were conducted in the lean exhaust of a stationary gas engine (MWM TCG V12, 600 kW) fed with biomethane, while establishing constant engine operation points with loads of 50 and 75%, resulting in exhaust temperatures of 485 °C (S.V.: 25,000 h^{-1}) and 465 °C (S.V.: 37,000 h^{-1}). The temperatures were recorded by K-type thermocouples positioned directly in front of the catalytic converter.

The performance of the catalysts was evaluated based on the conversion of the respective gas component according to the equation $X(i) = (y(i)_{in} - y(i)_{out})/y(i)_{in}$.

2.3 Mechanistic Studies of the CH$_2$O Oxidation

In-situ DRIFTS was performed using a FTIR spectrometer Tensor 27 (Bruker) equipped with a MCT detector and Praying Mantis optics (Harrick). For simultaneous surface and gas-phase analysis, the FTIR spectrometer mentioned in Sect. 2.1 was connected to the flow via a DRIFTS cell (Harrick). Gases were supplied as described in Sect. 2.2. Fresh catalyst powder (approx. 30 mg) was introduced into

the DRIFTS cell and pre-treated at 400 °C in synthetic air for 15 min. Subsequently, the sample was cooled to 350 °C, then the temperature was decreased to 50 °C in steps of 50 K, a background spectrum being recorded at each temperature level. At 50 °C, the sample was exposed to a gas mixture of 500 ppm CH$_2$O and N$_2$ (balance) with a total flow rate of 200 ml min^{-1} (STP). After saturation, it was flushed with a blend of 5 vol% O$_2$ and 95 vol% N$_2$ and spectra were recorded until no more changes occurred. Then, the sample was heated up to 350 °C in steps of 50 K under a constant gas flow. The spectra were collected between 800 and 3800 cm^{-1} with a resolution of 2 cm^{-1}, accumulating 400 scans per spectrum (5 min). The spectral data were processed using Opus Software (Bruker). Another series of experiments was performed following the same procedure but without dosing O$_2$. Moreover, in further experiments, the adsorption of the CH$_2$O (in N$_2$) was also carried out at -100 °C with subsequent flushing in 5 vol% O$_2$ and 95 vol% N$_2$.

Step function experiments were conducted on the laboratory test bench (Sect. 2.2) taking the best catalyst. The catalyst powder (200 mg) was pre-treated at 550 °C for 15 min in synthetic air and was subsequently cooled to 150 or 200 °C. Then, a gas mixture of 500 ppm CH$_2$O and N$_2$ (balance) was dosed into the bypass line, and additional runs were performed in the presence of 5 vol% O$_2$. The step function was realized by rapidly switching the gas flow from the bypass to the reactor. The total flow was always kept at 500 ml min^{-1}; gas phase analysis was carried out again using the FTIR spectrometer (Sect. 2.1).

3 Results and Discussion

3.1 Physico-Chemical Properties of the Fe$_2$O$_3$ Catalysts

The most important physico-chemical characteristics of the samples are demonstrated in Table 1, indicating BET surface areas from 5 to 25 m^2 g^{-1}. Based on these S_{BET} values, the samples are denoted by Fe5, Fe6, Fe8, Fe12 and Fe25 throughout this article. The mean pore diameters (d_{pore}) derived from the BJH model are between 32 and 52 nm

Table 1 Physico-chemical characteristics of the Fe$_2$O$_3$ samples

	S_{BET} m^{2}g^{-1}	d_{pore} nm	Phase –	d_{cryst} nm	T_{LT} °C	n_{CO2} µmol g^{-1}
Fe5	5	39	α-Fe$_2$O$_3$	63	265	2.3
Fe6	6	52	α-Fe$_2$O$_3$	77	275	5.6
Fe8	8	45	α-Fe$_2$O$_3$	61	237	3.2
Fe12	12	43	α-Fe$_2$O$_3$	61	260	5.0
Fe25	25	32	α-Fe$_2$O$_3$	26	230	6.6

(Table 1) indicating mesoporosity. The structural analyses by XRD (Fig. S1) and LRS (Fig. S2) confirm the exclusive presence of the hematite-type α-Fe$_2$O$_3$ phase in all the samples (Table 1). Additionally, it is obvious that the crystallite sizes (d_{cryst}) derived from the Scherrer equation decrease with increasing S_{BET}.

The redox properties were investigated by CO-TPR as shown for Fe25 by way of example (Fig. 1, left). It is known from the literature that the conversion of Fe$_2$O$_3$ with CO into CO$_2$ involves a three-step mechanism following the reduction sequence Fe$_2$O$_3$ → Fe$_3$O$_4$ → FeO → Fe [15]. The two initial steps coincide in the CO$_2$ feature at 350 °C as inferred from the cumulative oxygen release (Fig. 1, left) amounting to 11% (Fe$_3$O$_4$, area I) and 33% (FeO, Area II). The subsequent production of elemental Fe is indicated by the CO$_2$ evolution above 450 °C (Area III), resulting in the almost complete removal of oxygen from the Fe$_2$O$_3$ at 850 °C (96%). In total, 18.8 mmol g^{-1} of oxygen is removed. Additionally, the CO-TPR profiles reveal a minor pre-peak at low temperatures (T_{LT}), which is observed at 230 °C for Fe25, whereas the remaining samples show higher T_{LT} values shifting to 275 °C. Since this CO$_2$ formation occurs at the beginning of the TPR, it is assumed that surface and subsurface oxygen species are predominately involved. For a rough estimation of the amount of oxygen required for a monolayer, the surface area of O^{2-} ($6.16 \cdot 10^{-20}$ m^2) [18], the mass and the BET surface area of each sample are used. With this value (14–67 μmol) and the amount of oxygen released during the low-temperature CO$_2$ formation ($n_{O,LT}$, 17–67 μmol), it is deduced that both quantities are in the same order of magnitude, indicating the participation of surface and/or subsurface oxygen. Thus, T_{LT} is taken in Sect. 3.2 as a feature to express the reducibility of the sample surfaces.

The number of active Fe sites is estimated from the uptake of CO$_2$ determined by CO$_2$-TPD (n_{CO2}, Table 1). Note that before the TPD, the samples were pre-treated at 550 °C, resulting in some dehydroxylation of the surface that partially changed the coordination sphere of the surface Fe atoms, whereas the adsorption of CO$_2$ led to the formation of carbonate surface complexes [19]. The CO$_2$-TPD profile is shown by way of example for Fe25 (Fig. 1, right), demonstrating two prominent features at 100 and 400 °C that are associated with the decomposition of differently coordinated carbonato entities [19]. The n_{CO2} data range from 2.3 to 6.6 μmol g^{-1}, roughly increasing with the BET surface area.

3.2 Oxidation Performance And Structure–Activity Correlations Of The Fe2O3 Catalysts

The performance of the powder catalysts during the simultaneous CH$_2$O and CH$_4$ oxidation was evaluated in a model lean gas engine exhaust gas. Figure 2 (left) shows that Fe25 exhibits the highest conversion of CH$_4$, starting at 400 °C and reaching 22% at 550 °C. By contrast, the oxidation of CH$_2$O occurs at far lower temperatures for all catalysts
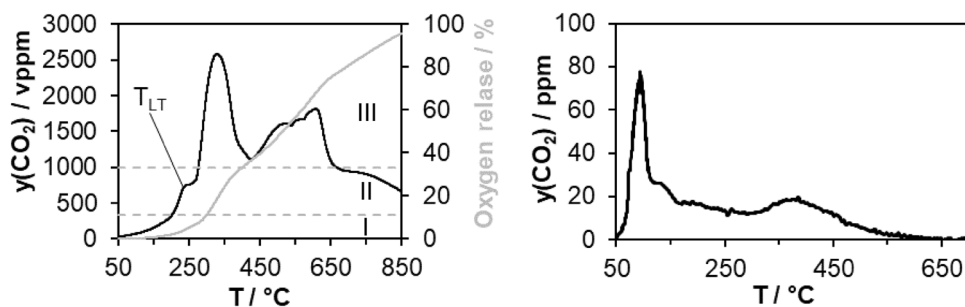

Fig. 1 CO-TPR of Fe25 with cumulative oxygen release in the form of CO$_2$ (left) and CO$_2$-TPD of Fe25 (right). CO-TPR conditions: m = 150 mg, F = 150 ml min^{-1} (STP), y(CO) = 3000 ppm, N$_2$ balance, β = 10 K min^{-1}. CO$_2$-TPD conditions: m = 500 mg, F = 150 ml min^{-1} (STP); saturation: y(CO$_2$) = 3000 ppm, N$_2$ balance; TPD: N$_2$ flow, β = 20 K min^{-1}

Fig. 2 Conversion of CH$_4$ (left) and CH$_2$O (right) on the Fe$_2$O$_3$ catalysts (Fe6 (□), Fe5 (X), Fe8 (△), Fe12 (◇), Fe25 (○). Conditions: y(CH$_4$) = 1000 ppm, y(CH$_2$O) = 100 ppm, y(O$_2$) = 5 vol%, y(H$_2$O) = 10 vol%, N$_2$ balance, S.V. = 150,000 h^{-1} (STP)
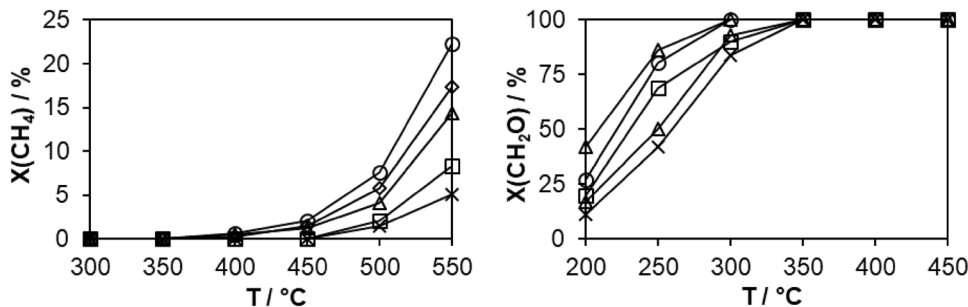
(Fig. 2, right), whereas Fe8 and Fe25 exhibit the highest activity, with total conversion at just 300 °C. The oxidation of CH_2O and CH_4 results in the selective production of CO_2 at 250 °C and above, while a minor amount of CH_3OH (< 10 ppm) is also formed at 200 °C, corresponding to a selectivity of 10%; the mechanism of the CH_3OH production is examined in Sect. 3.3. The performance of the samples remains the same upon a following catalytic run and after exposure to the model exhaust for 1 h at 550 °C.

When the activity (Fig. 2) is coupled with the physicochemical properties of the catalysts (Table 1), it is clear that high BET surface areas and small crystallite sizes enhance the CH_4 oxidation, as shown in Fig. S3 (left). This may be related to the number of active sites, which increases as the surface area rises. Indeed, the CH_4 oxidation rates related to each surface area are similar; at 550 °C, for instance, they range from 21 to 45 μmol m^{-2} h^{-1}, substantiating the importance of a large BET surface area to achieve high conversion levels. However, Fig. 3 (left) suggests that the surface reducibility of the catalysts overlaps with the effect of the surface area. The diagram shows that the CH_4 oxidation activity increases if the T_{LT} value during CO-TPR is decreased, indicating the relevance of the availability of active surface oxygen. It may be speculated that the oxygen species involved exist in the form of FeO_6 entities, which are the thermodynamic coordination polyhedrons of α-Fe_2O_3.

With the amount of active surface oxygen, derived from CO-TPR (Sect. 3.1), and the conversion rate of CH_4 ($X_{CH4,550\,°C}$), taken from Fig. 2, the turnover frequency (TOF) of the active FeO_x sites is roughly estimated for the CH_4 oxidation at 550 °C (TOF = $\dot{n}_{CH4,0} \cdot X_{CH4,550\,°C}/n_{O,LT}$). As a result, the TOF values of the Fe_2O_3 catalysts range from $1 \cdot 10^{-3}$ to $7 \cdot 10^{-3}$ s^{-1}. Compared to Pt sites, for which TOF data at 370 °C between $7 \cdot 10^{-3}$ and $360 \cdot 10^{-3}$ s^{-1} are reported [20], it is clear that the active Fe sites still exhibit inferior CH_4 oxidation efficiency.

Moreover, similarly to the conversion of CH_4, the CH_2O oxidation is also enhanced by a rising BET surface area (Fig. S3, right). Figure 3 (right) also indicates a relation between rising CH_2O conversion and an increasing uptake of CO_2. The relevance of the CO_2 adsorption for the CH_2O oxidation performance of the Fe_2O_3 catalysts lies in the role

of surface formates and carbonates in the reaction mechanism; this is discussed in detail in Sect. 3.4. CH_2O and CO_2 are expected to adsorb on the same surface sites due to their structural similarity.

3.3 Upscaling the Best Catalyst

Since Fe25 performs best for the simultaneous oxidation of CH_2O and CH_4 (Fig. 2), this powder sample was selected for the first level of upscaling, a 1″ cordierite monolith. For these catalytic tests, a more realistic model exhaust gas was used comprising CH_2O, CH_4, CO and NO, and higher proportions of H_2O and CO_2 (each 12 vol%). The reactant load of the catalyst was clearly higher for the monolith as compared to the powder, i.e., 143 vs. 723 $mg(CH_4)$ g^{-1} s^{-1}, and 27 vs. 90 $mg(CH_2O)$ g^{-1} s^{-1}. As a result (Fig. 4), the monolith showed markedly lower conversions of CH_4 and CH_2O. For instance, only 7% of CH_4 is converted at 550 °C (powder: 22%), whereas the amount of CH_2O converted at 250 °C is 13% (powder: 80%); almost complete CH_2O oxidation occurs at 400 °C and above. The monolith also exhibits CO oxidation, with a maximum removal of 84% (550 °C), whereas only little oxidation of NO takes place, the maximum NO_2 yield being 13% at 500 °C.
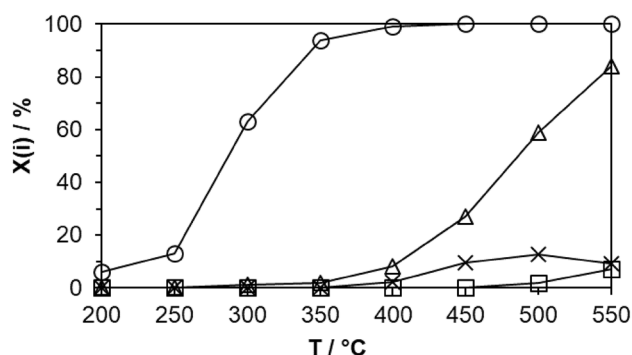
Fig. 4 Conversion of CH_2O (○), CO (Δ), NO (X) and CH_4 (□) on the 200 cpsi monolith coated with Fe25 (100 g l^{-1}). Conditions: $y(CH_4)$ = 1500 ppm, $y(CH_2O)$ = 100 ppm, $y(CO)$ = 600 ppm, $y(NO)$ = 250 ppm, $y(O_2)$ = 5 vol%, $y(H_2O)$ = 12 vol%, $y(CO_2)$ = 12 vol%, N_2 balance, S.V. = 65,000 h^{-1} (STP)

Fig. 3 Relation of the CH_4 conversion at 550 (▲) and 500 °C (●) with the T_{LT} value during CO-TPR (left) and relation of the CH_2O conversion at 250 (Δ) and 200 °C (○) with the CO_2 uptake inferred from CO_2-TPD (right); the lines are a guide for the eyes
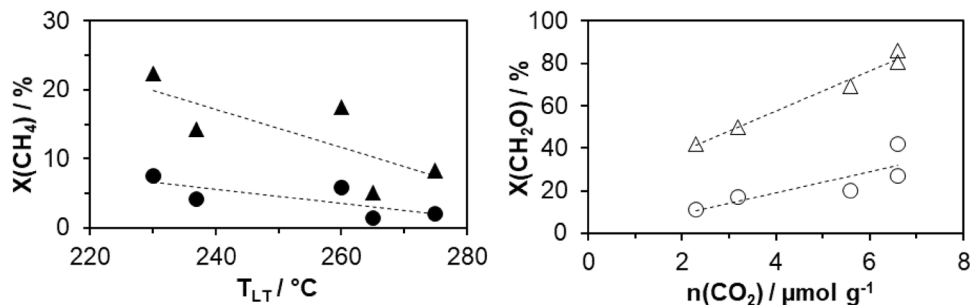
Due to the high CH_2O oxidation efficiency, the catalyst was further upscaled to the real converter level using a 200 cpsi honeycomb substrate (D: 390 mm, L: 450 mm, 85 g l^{-1}) and was evaluated on the stationary biomethane engine (Sect. 2.2). The two engine operation points that were established resulted in temperatures of 485 °C for a 50% load and 465 °C for a 75% load. The reactant load of the catalyst was 580 mg(CH_4) g^{-1} s^{-1}, 239 mg(CO) g^{-1} s^{-1} and 27 mg(CH_2O) g^{-1} s^{-1} for a 50% engine load and 843 mg(CH_4) g^{-1} s^{-1}, 348 mg(CO) g^{-1} s^{-1} and 40 mg(CH_2O) g^{-1} s^{-1} for a 75% engine load. Figure 5 shows that in the fresh state, the catalyst oxidized CH_2O completely for both engine loads, whereas the CO conversion amounted to 80% (485 °C) and 60% (465 °C). This high efficiency in the case of CH_2O and CO is in line with the results from the laboratory test bench (Fig. 4). Note that no significant CH_4 oxidation appeared; this was related to the relatively low exhaust temperatures. Moreover, it should be mentioned that the conversion of CH_2O and CO dropped within 21 h, but remained constant after that. The initial decrease in activity is typical for the deposition of ash components on the catalyst, originating from the motor oil [21]. No SO_X was detected in the exhaust gas by the FTIR spectrometer (detection limit of approx. 1 ppm). However, even low concentrations in the ppb range might cause a significant accumulation and some deactivation of the catalytic converter. Indeed, SEM–EDX analyses revealed deposits, particularly in the upstream area of the converter, mainly consisting of Ca, Zn, Si, S and P.

In the literature, commercial Pt/Pd catalysts are reported to completely convert CH_2O and CO in gas engine exhaust systems at a very similar temperature (475 °C), but with double the gas hourly space velocity, GHSV (80,000–100,000 h^{-1}) [22]. CH_4 is not converted.

3.4 Mechanism of CH_2O Oxidation

The mechanism of CH_2O oxidation, including CH_3OH evolution during CH_2O light-off, was investigated with Fe25, which is the best catalyst tested (Sect. 3.2). The in-situ DRIFTS studies were performed in a broad temperature range from 50 to 350 °C to provide a comprehensive understanding of the surface reactions. For clarity, selected spectral ranges from 2600 to 3800 cm^{-1} and 900 to 1800 cm^{-1} are depicted in Fig. 6, while all the DRIFT spectra are illustrated in Fig. S4.

Fig. 5 Conversion of CH_2O (○) and CO (△) for the 200 cpsi honeycomb coated with Fe25 (85 g l^{-1}) in the exhaust system of the biomethane engine MWM TCG V12 (dashed lines: 50% load, solid lines: 75% load)
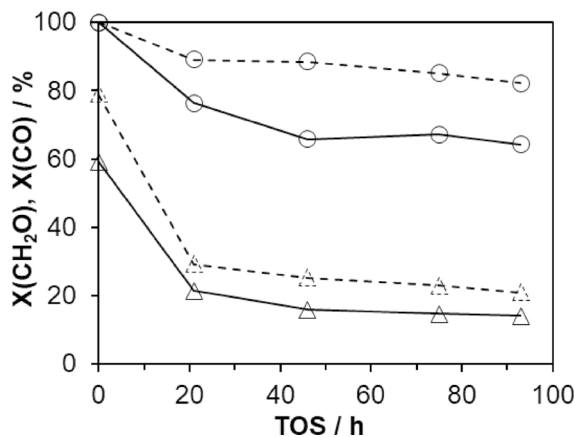
Parameters	Engine load	
	50 %	75 %
T / °C	485	465
S.V. / h^{-1}	25,000	37,000
y(CH_4) / ppm	2800	2500
y(CH_2O) / ppm	75	70
y(CO) / ppm	630	660
y(NO_x) / ppm	120	130
y(O_2) / vol%	7	
y(H_2O) / vol%	12	
y(CO_2) / %	10	

Fig. 6 DRIFT spectra of the Fe25 catalyst after CH_2O exposure (50 °C) and subsequent flushing with N_2 at 50 °C (grey), 100 °C (dashed grey), 150 °C (dark grey), 200 °C (dashed line) and 250 °C (solid line). Conditions: y(CH_2O) = 500 ppm, y(O_2) = 5 vol%, N_2 balance, F = 200 ml min^{-1} (STP)
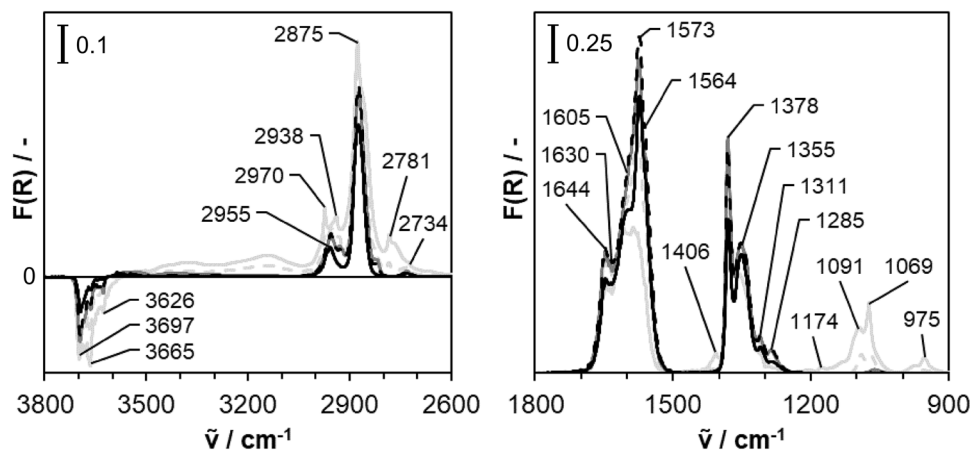
Figure 6 shows the DRIFTS data recorded after the CH_2O/O_2 exposure at 50 and 100 °C, indicating the formation of $[CH_2O]_n$ oligomers on the catalyst surface associated with the bands at 1406 (δ_{CH2}) and 2938 cm^{-1} (ν_{CH2}) [23, 24]. These species are clearly distinguished from the related polyoxymethylene (POM) entities, which are reported to form bands at 1470 (δ_{CH2}) and 2921 cm^{-1} (ν_{CH2}) [25]. Additionally, dioxymethylene moieties are not produced due to the absence of features at 1473 (δ_{CH2}) and 2882 cm^{-1} (ν_{CH2}) [26]. The oligomerization of CH_2O occurs in the presence of bases with the consumption of OH species and the formation of H_2O, which is partially adsorbed on the catalyst, as indicated by the DRIFTS band at 1644 cm^{-1} (δ_{HOH}) [19, 23, 27]. The OH groups required for the formation of the $[CH_2O]_n$ oligomers are provided by the surface of the catalyst. The consumption of the OH sites is substantiated by bands with a negative formal charge between 3550 and 3700 cm^{-1} (ν_{OH}). Moreover, methoxy (OCH_3) and bidentate formate species (HCO_2) appear [23, 24, 26, 28]. The former are related to the bands at 2970 (ν_{CH2}), 2860 (ν_{CH2}), 1174 (ν_{CO}), 1091 ($\nu_{a,CO}$) and 1069 cm^{-1} (ν_{CO}). Due to the same temporal progression, the bands at 2981 (ν_{CH2}) and 975 cm^{-1} (ν_{CO}) are also tentatively assigned to methoxy groups. By contrast, the formates are associated with the intense features at 1378 (δ_{CH}) and 1355 cm^{-1} ($\nu_{s,COO}$). In addition, carbonate species appear initially at 100 °C, as deduced from the features at 1573 (ν_{CO}), 1311 ($\nu_{as,OCO}$) and 1285 ($\nu_{as,COO}$) cm^{-1} [19]. The assignments of all the DRIFTS bands are summarized in Table S1.

At 150 °C, the intensity of the bands identifying methoxy groups decreases and CH_3OH is detected in the gas phase (Fig. S5). The bands of formate species increase at a temperature of 150 °C. Above 200 °C, methoxy groups are no longer observed, and the intensity of the formate bands decreases as the temperature rises. Simultaneously (at 200 °C and above), the intensity of the OH bands increases between 3550 and 3700 cm^{-1} (ν_{OH}). Surface OH groups are partially regenerated by the reaction of formate species and H_2O, leading to the formation of formic acid (HCOOH). The H_2O required comes from the CH_2O oligomerization and is also present in trace amounts in the feed due to the CH_2O supply. It should be noted that in real exhaust gas, a large excess of H_2O is available. Traces of HCOOH and H_2 are detected in the gas phase at 200 °C and above using FTIR and gas chromatography, respectively. The unstable HCOOH partly decomposes into H_2 and CO_2. In addition, above 200 °C strong carbonate bands appear at 1573 (ν_{CO}), 1311 ($\nu_{as,OCO}$) and 1285 ($\nu_{as,COO}$) cm^{-1} [19, 29, 30] and adsorbed H_2O (1644 cm^{-1} (δ_{OH})) [19, 23, 27] occurs, formed by the oxidation of CH_3OH or formates, or HCOOH. Apart from the formation of H_2O, surface OH groups are also reformed, and at 300 °C they are fully regenerated. Significant thermal decomposition of the carbonate species occurs at 250 °C and

above, as indicated by the decrease in the corresponding DRIFTS features (Fig. S5) as well as the detection of gaseous CO_2. At 350 °C, no bands are found any longer due to the enhanced desorption of the surface species, indicating that the catalytic cycle is closed.

For reference purposes, DRIFT spectra (Fig. S6) were recorded after CH_2O exposure at -100 °C, providing bands at 2980 (ν_{CH2}), 2921 (ν_{CH2}), 2786 (ν_{CH2}), 1470 (δ_{CH2}), 1433 (ω_{CH2}), 1382 (ω_{CH2}), 1239 (ν_{CO}), 1104 (ν_{CO}) and 947 cm^{-1} (ν_{CO}), which are all assigned to adsorbed POM [25, 26]. The iron-oxide-assisted polymerization of CH_2O is known from the literature, while Brønsted acid OH groups on SiO_2 and Brønsted basic sites on MgO are discussed as active sites. Meanwhile, there is a debate on the nature of the sites of Fe_2O_3 catalysts [23, 26, 31]. Since Fig. S6 reveals negative bands between 3550 and 3700 cm^{-1} (ν_{OH}) during the POM formation, it is suggested that at least OH sites of Fe25 participate in the CH_2O polymerization. Additionally, the DRIFT spectra remain unchanged if the temperature is subsequently increased to 0 °C, indicating that the POM moieties are stable. However, when the temperature is further raised to 50 °C, the rapid and complete decomposition of POM takes place (Fig. S4) in line with the DRIFTS investigation reported above for CH_2O exposure at 50 °C (Fig. 6). This clearly demonstrates that CH_2O does not exist as a stable adsorbate on the Fe25 sample in the temperature range investigated (-100–350 °C).

From the DRIFTS findings, the mechanism for the lean CH_2O oxidation on α-Fe_2O_3 (Fe25) is deduced (Fig. 7), primarily addressing conversion below approx. 350 °C, including the cold start phase of gas engines. The first reaction step involves the adsorption of CH_2O, resulting in POM species below 50 °C and $[CH_2O]_n$ oligomers at 50 °C subsequently forming dioxymethylene (II); the latter is not detected by DRIFTS, which may be related to its high reactivity and/or the superimposition of its vibration bands by those of the related $[CH_2O]_n$ oligomers. Two adjacent dioxymethylene species are assumed to react to formate and methoxy species in the form of a Cannizzaro-type reaction (III–IV). In the subsequent hydrolysis of the methoxy groups, CH_3OH is released at 150 °C and some OH surface groups (V) are reformed, as observed with DRIFTS. Overall, the Cannizzaro mechanism involves the reaction of two CH_2O molecules with four OH groups of the catalyst surface, yielding gaseous CH_3OH and a formate adsorbate [32]. Above 200 °C, the hydrolysis of formates occurs, leading to the production of HCOOH, detected in the gas phase, and the further reforming of OH groups (VI), as indicated by increase in the OH stretching vibration range and a simultaneous decrease in the formate bands. However, HCOOH decomposes into CO_2 and H_2, which is partly oxidized to yield H_2O. Likewise, above 200 °C the oxidation of CH_3OH into CO_2 and H_2O starts, which is verified by the disappearance
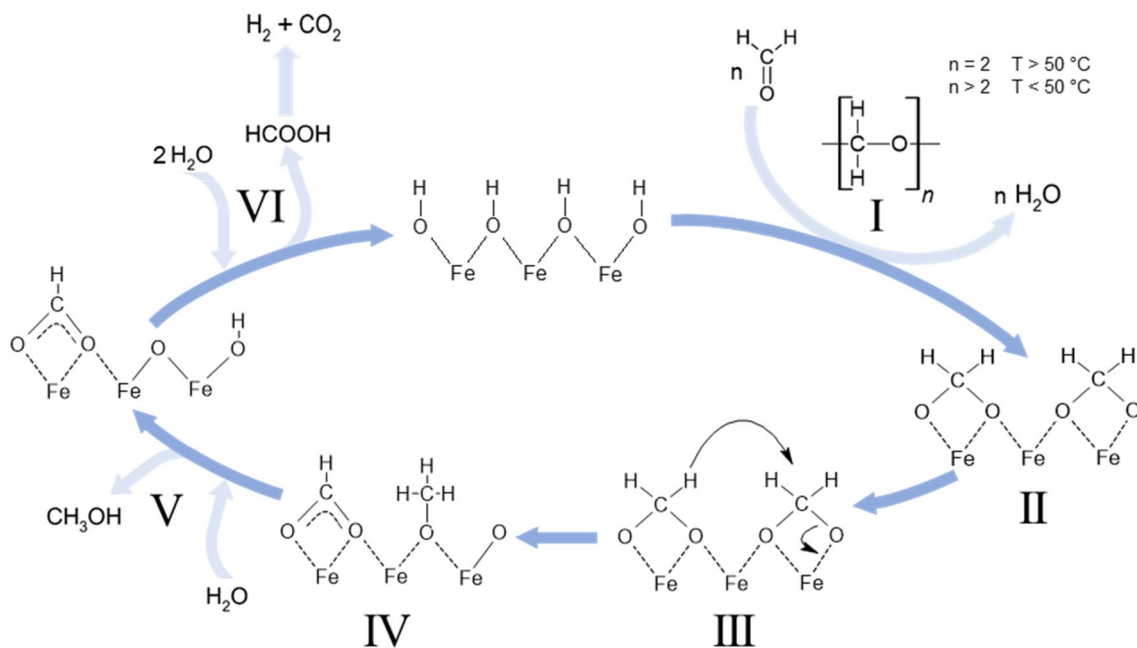
Fig. 7 Mechanism of CH_2O conversion on α-Fe_2O_3 catalyst according to a Cannizzaro-type

of the methoxy groups with a simultaneous increase in the gas phase concentration of CO_2. A separate experimental study (in a tubular quartz glass reactor, Sect. 2.2) examining CH_3OH oxidation on Fe25 was performed under the same conditions to confirm this statement. An initial conversion of CH_3OH to CO_2 was evident at 200 °C. Complete conversion already occurred at 275 °C. Since no methoxy groups were present on the surface above 200 °C, the carbonates that are present are primarily formed by the decomposition of formates, which desorb up to 350 °C. Finally, based on the DRIFTS experiments, it cannot be completely excluded that some CH_2O species are directly oxidized to create formate, although this route does not explain the appearance of methoxy and CH_3OH species.

Moreover, the O_2 formally required for the CH_2O oxidation according to Eq. 2 is likely involved in the follow-up oxidation of CH_3OH and $HCOOH$ (or its decomposition product H_2) on the Fe_2O_3 catalyst.

An additional mechanistic investigation of the CH_2O oxidation involved a step function experiment, in which Fe25 was immediately exposed at 150 °C to a gas flow composed of 500 ppm CH_2O and 5 vol% O_2 (N_2 balance). The temporal progression of the relative fractions (molar) of the reactants related to the inlet proportion of CH_2O is depicted in Fig. S7. In the first 200 s of the experiment, the incorporation of carbon species is evident (C balance significantly below 1). An initial formation of CH_3OH is also observed, with a peak at an exposure time of 365 s, corresponding to a yield of 45%. After 1500 s, neither the incorporation of carbon nor the conversion of CH_2O is observed any longer. During the total

CH_2O exposure lasting 1300 s, 48 μmol CH_2O is converted with the formation of 23 μmol CH_3OH and the accumulation of 26 μmol carbon. After this experiment, the catalyst was heated to 550 °C in a flow of synthetic air, resulting in the release of 27 μmol CO_2. Similar results were obtained in the step function study performed at an exposure temperature at 200 °C (Figure S8). From the reaction mechanism suggested in Fig. 7, it is inferred that the accumulated carbon is related to formate species. This interpretation is in line with the stoichiometry of the Cannizzaro-type mechanism involving the conversion of two CH_2O molecules (here: 48 μmol) into one CH_3OH (here: 23 μmol) and one formate species (here: 26 μmol). It should be stated that according to DRIFTS studies (Fig. 6), formates only start decomposing above 150 °C, leading to this accumulation in the step function experiment. However, as a consequence of the lacking formate release, the surface of the catalyst is increasingly covered by the formates, while the OH groups are progressively consumed, diminishing the conversion of CH_2O and the production of CH_3OH as observed in the step function investigation.

4 Conclusions

Out of the systematic series of five α-Fe_2O_3 samples, the catalyst powder with the highest BET surface area (Fe25) showed the best CH_4/CH_2O oxidation performance under lean conditions. The investigations showed that α-Fe_2O_3 catalysts are suitable for the oxidation of lean CH_2O (full conversion) and CH_4 (up to 25%) above 300 and 550 °C,

respectively. Structure–activity relations indicated that for CH_4 conversion, the relevant properties driving the catalytic performance are a high BET surface area corresponding to a multitude of active sites, a small crystallite size and the high reducibility of the catalyst surface or availability of surface oxygen. By contrast, for the oxidation of CH_2O, the total CO_2 adsorption capacity according to the availability of OH adsorption sites is crucial. In accordance with the suggested Cannizzaro-type mechanism, these OH surface groups are involved in the conversion of CH_2O into CH_3OH and formate species between 100 and 200 °C, including a CH_3OH selectivity up to 45%. Thus, CH_3OH has to be considered as a significant secondary pollutant, particularly during the cold start phase of the gas engines. However, above 250 °C, CH_3OH is no longer emitted, probably due to the inhibition of the Cannizzaro mechanism, associated with the enhanced oxidation of the methoxy species. Furthermore, above 200–250 °C, formates and carbonates become the predominating surface species, therefore their thermal removal is assumed to affect the overall CH_2O oxidation rate.

The Fe25 sample was upscaled to the honeycomb level including a 1″ monolith for laboratory tests and a 390×450 mm substrate for tests in a real gas engine exhaust system. These investigations with the monolithic catalysts indicated a clearly lower CH_2O/CH_4 oxidation performance compared to the studies with the catalyst powder. This is related to the higher reactant load of the monoliths. The monoliths also exhibited considerable CO oxidation activity. In the gas engine exhaust system, the catalyst revealed substantial CH_2O oxidation, with full conversion at 460 °C. By contrast, the real exhaust temperatures were too low to activate the CH_4 oxidation on the monolith. The overall activity of the monolith is lower compared to precious metal catalysts [22, 33]. However, it can be postulated that by moderately increasing the residence time, similar conversions of CO and CH_2O can be reached. Higher conversion levels might also be achieved with the Fe-based converter by improving the washcoat loading. Its use in stationary engines with higher exhaust temperatures between approx. 500 and 550 °C is also advantageous, particularly for the effective conversion of CH_4.

The findings of the current paper can be used to enhance the performance of iron oxide catalysts. This could be achieved in further investigations by adding thermal promoters (e.g., tungsten and lanthanum) and electronic promoters (e.g., alkali (earth) metals).

Supplementary Information The online version contains supplementary material available at https://doi.org/10.1007/s11244-022-01730-2.

References

1. Yoon SH, Lee CS (2011) Experimental investigation on the combustion and exhaust emission characteristics of biogas–biodiesel dual-fuel combustion in a CI engine. Fuel Process Technol 92:992–1000. https://doi.org/10.1016/j.fuproc.2010.12.021

2. Liebetrau J, Clemens J, Cuhls C et al (2010) Methane emissions from biogas-producing facilities within the agricultural sector. Eng Life Sci 10:595–599. https://doi.org/10.1002/elsc.201000070

3. Bauer M, Wachtmeister G (2009) Formation of formaldehyde in lean-burn gas engines. MTZ Worldw 70:50–57. https://doi.org/10.1007/BF03226970

4. Corrêa SM, Arbilla G (2005) Formaldehyde and acetaldehyde associated with the use of natural gas as a fuel for light vehicles. Atmos Environ 39:4513–4518. https://doi.org/10.1016/j.atmosenv.2005.03.042

5. Pocoroba E, Pettersson LJ, Agrell J et al (2001) Exhaust gas catalysts for heavy-duty applications: influence of the Pd particle size and particle size distribution on the combustion of natural gas and biogas. Top Catal 16(17):407–412. https://doi.org/10.1023/A:1016637805194

6. Li C, Shen Y, Jia M et al (2008) Catalytic combustion of formaldehyde on gold/iron-oxide catalysts. Catal Commun 9:355–361. https://doi.org/10.1016/j.catcom.2007.06.020

7. Choudhary TV, Banerjee S, Choudhary VR (2002) Catalysts for combustion of methane and lower alkanes. Appl Catal A 234:1–23. https://doi.org/10.1016/S0926-860X(02)00231-4

8. Arnone S, Bagnasco G, Lisi L et al (1998) Catalytic combustion of methane over transition metal oxides. Stud Surf Sci Catal 119:65–70. https://doi.org/10.1016/S0167-2991(98)80409-6

9. Fan Z, Fang W, Zhang Z et al (2018) Highly active rod-like Co_3O_4 catalyst for the formaldehyde oxidation reaction. Catal Commun 103:10–14. https://doi.org/10.1016/j.catcom.2017.09.003

10. Shi C, Wang Y, Zhu A et al (2012) $Mn_xCo_3{-}xO_4$ solid solution as high-efficient catalysts for low-temperature oxidation of formaldehyde. Catal Commun 28:18–22. https://doi.org/10.1016/j.catcom.2012.08.003

11. Park PW, Ledford JS (1998) The influence of surface structure on the catalytic activity of alumina supported copper oxide catalysts. Oxidation of carbon monoxide and methane. Appl Catal B 15:221–231. https://doi.org/10.1016/S0926-3373(98)80008-8

12. Pei J, Han X, Lu Y (2015) Performance and kinetics of catalytic oxidation of formaldehyde over copper manganese oxide catalyst. Build Environ 84:134–141. https://doi.org/10.1016/j.buildenv.2014.11.002

13. Tepluchin M, Pham DK, Casapu M et al (2015) Influence of single- and double-flame spray pyrolysis on the structure of MnO_x/γ-Al_2O_3 and FeO_x/γ-Al_2O_3 catalysts and their behaviour in CO removal under lean exhaust gas conditions. Catal Sci Technol 5:455–464. https://doi.org/10.1039/c4cy00727a

14. Waglöhner S, Reichert D, Leon-Sorzano D et al (2008) Kinetic modeling of the oxidation of CO on Fe_2O_3 catalyst in excess of O_2. J Catal 260:305–314. https://doi.org/10.1016/j.jcat.2008.09.018

15. Wagloehner S, Baer JN, Kureti S (2014) Structure–activity relation of iron oxide catalysts in soot oxidation. Appl Catal B 147:1000–1008. https://doi.org/10.1016/j.apcatb.2013.09.049

16. Wagloehner S, Kureti S (2012) Study on the mechanism of the oxidation of soot on Fe_2O_3 catalyst. Appl Catal B 125:158–165. https://doi.org/10.1016/j.apcatb.2012.05.032

17. Schwertmann U, Cornell RM (2008) Iron oxides in the laboratory: preparation and characterization. Wiley-VCH, Hoboken

18. Müller U (2009) Anorganische Strukturchemie, 6., aktualisierte Aufl., unveränd Nachdr. Studienbücher Chemie. Vieweg + Teubner, Wiesbaden

19. Breyer C, Reichert D, Seidel J et al (2015) Kinetic modeling of the adsorption and desorption of CO_2 on α-Fe_2O_3. Phys Chem Chem Phys 17:27011–27018. https://doi.org/10.1039/c5cp04671h

20. Hicks R, Qi H, Young M et al (1990) Effect of catalyst structure on methane oxidation over palladium on alumina. J Catal 122:295–306. https://doi.org/10.1016/0021-9517(90)90283-P

21. Gallopoulos NE, Summers JC, Klimisch RL (1973) effects of engine oil composition on the activity of exhaust emissions oxidation catalysts. SAE Technical Paper. https://doi.org/10.4271/730598

22. Stolze B, Hartmann I (2020) Zeitliche darstellung des alterungsverhaltens eines oxidationskatalysators in einem biogas-BHKW. Chem Ing Tec 92:782–787. https://doi.org/10.1002/cite.201900152

23. Davydov A (2003) Molecular Spectroscopy of Oxide Catalyst Surfaces. Wiley

24. Busca G (1980) Infrared study of methanol, formaldehyde, and formic acid adsorbed on hematite. J Catal 66:155–161. https://doi.org/10.1016/0021-9517(80)90017-2

25. Li Y, Zhou T, Chen Z et al (2011) Non-isothermal crystallization process of polyoxymethylene studied by two-dimensional correlation infrared spectroscopy. Polymer 52:2059–2069. https://doi.org/10.1016/j.polymer.2011.03.007

26. Busca G, Lamotte J, Lavalley JC et al (1987) FT-IR study of the adsorption and transformation of formaldehyde on oxide surfaces. J Am Chem Soc 109:5197–5202. https://doi.org/10.1021/ja00251a025

27. Al-Mashta F, Sheppard N, Lorenzelli V et al (1982) Infrared study of adsorption on oxygen-covered α-Fe_2O_3: bands due to adsorbed oxygen and their modification by co-adsorbed hydrogen or water. J Chem Soc, Faraday Trans 1(78):979. https://doi.org/10.1039/F19827800979

28. Bowker M, Gibson EK, Silverwood IP et al (2016) Methanol oxidation on Fe_2O_3 catalysts and the effects of surface Mo. Faraday Discuss 188:387–398. https://doi.org/10.1039/c5fd00225g

29. Baltrusaitis J, Jensen JH, Grassian VH (2006) FTIR spectroscopy combined with isotope labeling and quantum chemical calculations to investigate adsorbed bicarbonate formation following reaction of carbon dioxide with surface hydroxyl groups on Fe_2O_3 and Al_2O_3. J Phys Chem B 110:12005–12016. https://doi.org/10.1021/jp057437j

30. Wu JCS, Huang C-W (2010) In situ DRIFTS study of photocatalytic CO_2 reduction under UV irradiation. Front Chem Eng China 4:120–126. https://doi.org/10.1007/s11705-009-0232-3

31. Brown N (1967) Polymerization of formaldehyde. J Macromol Sci: A - Chem 1:209–230. https://doi.org/10.1080/10601326708053967

32. Kürti L, Czakó B (2009) Strategic applications of named reactions in organic synthesis: Background and detailed mechanisms; 250 named reactions, [Nachdr.]. Elsevier Acad Press, Amsterdam

33. Gremminger A, Pihl J, Casapu M et al (2020) PGM based catalysts for exhaust-gas after-treatment under typical diesel, gasoline and gas engine conditions with focus on methane and formaldehyde oxidation. Appl Catal B 265:118571. https://doi.org/10.1016/j.apcatb.2019.118571

34. Rochester CH, Topham SA (1979) Infrared studies of the adsorption of probe molecules onto the surface of haematite. J Chem Soc, Faraday Trans 1(75):1259. https://doi.org/10.1039/F19797501259

35. Busca G, Rossi PF (1983) FT-IR spectroscopic and calorimetric characterization of the adsorbed forms of water on α-Fe_2O_3 obtained by thermal decomposition of α-FeOOH. Mater Chem Phys 9:561–570. https://doi.org/10.1016/0254-0584(83)90056-1